# Three dimensional quantification of soil hydraulic properties using X-ray Computed Tomography and image based modelling

**Author list:** Saoirse R. Tracy[1$], Keith R. Daly[2$], Craig J. Sturrock[1], Neil M. J. Crout[1], Sacha J. Mooney[1], Tiina Roose[2§]

**Author affiliations:**

[1] School of Biosciences, University of Nottingham, Sutton Bonington Campus, Leicestershire, LE12 5RD.

[2] Bioengineering Sciences Research Group, Faculty of Engineering and Environment, University of Southampton, University Road, SO17 1BJ.

[$] These authors are joint lead authors

[§] Corresponding author: Bioengineering Sciences Research Group, Faculty of Engineering and Environment, University of Southampton, University Road, SO17 1BJ Southampton, United Kingdom, email: t.roose@soton.ac.uk

**Key Points:**

- X-ray Computed Tomography is used to image water distribution in soil.
- 3D Computed Tomography images are combined with image based modelling.
- Unsaturated hydraulic conductivity and the water release characteristic are obtained.

## 1. Abstract

We demonstrate the application of a high-resolution X-ray Computed Tomography (CT) method to quantify water distribution in soil pores under successive reductive drying. We focus on the wet end of the water release characteristic (WRC) (0 to -75 kPa) to investigate changes in soil water distribution in contrasting soil textures (sand and clay) and structures (sieved and field structured), to determine the impact of soil structure on hydraulic behaviour. The 3D structure of each soil was obtained from the CT images (at a 10 $\mu$m resolution). Stokes equations for flow were solved computationally for each measured structure to estimate hydraulic conductivity. The simulated values obtained compared extremely well with the measured saturated hydraulic conductivity values. By considering different sample sizes we were able to identify that the smallest possible representative sample size which is required to determine a globally valid hydraulic conductivity.



**Keywords:** Matric potential; soil pores; water release characteristic; X-ray Computed Tomography; image based homogenisation.


**Abbreviations:**

(3D) - 3-dimensional

(CT) - Computed Tomography

(ROI) - Region of interest

(WRC) – Water release characteristic

(WFP) – Water filled pores

(AFP) – Air filled pores

(REV) -Representative elementary volume

**Short title for page headings:** Three-dimensional quantification of soil hydraulic properties

## 2. Introduction

Understanding the dynamic nature of water movement through, and storage within, soil is of fundamental importance for most of its functions. A more detailed knowledge of how soil structure influences soil water distribution and subsequently availability to plants is needed to inform soil management practices and thus contribute to efforts in increasing crop yields for an expanding global population. However, to truly understand how water moves through soil and is retained in soil pores whilst undergoing drying, non-destructive measurements of the soil aggregate geometries and pore structure are needed. The use of X-ray Computed Tomography (CT) to examine the 3D soil pore structure is rapidly gaining pace [*Helliwell et al.,* 2014; *Mooney et al.,* 2012]. The ability to segment water from a greyscale CT image remains challenging due to limitations in the phase separation achievable with regular detectors in benchtop CT scanners. Segmentation of fluids in alternative porous media such as glass beads has been previously described in the literature [*Haugen et al.*, 2014; *Iassonov et al.*, 2009]. However, due to the more complex, heterogeneous structure of soil and the associated challenges faced during image acquisition this brings, these segmentation techniques cannot always be readily applied to the segmentation of soil phases in X-ray CT images [*Houston et al.*, 2013]. Yet, Crestana *et al.* [1985] highlighted the potential of CT for investigating water movement through soil by quantifying the vertical and lateral water flows

69 in 3D. By using dual energy tomography Rogasik *et al.* [1999] showed it is possible to
70 quantify soil water, pore space and bulk density. Mooney [2002], compared dry and moist
71 samples and developed an imaging method to separate water from the bulk soil in
72 undisturbed soil cores albeit at a coarse resolution (0.5 mm) using a medical CT scanner.
73 Water flow characteristics were well matched to macropore structure, with*circa* 90% of
74 macropore space active in water transport in a sandy clay texture, compared to *circa* 50% in
75 the sandy loam soil. Wildenschild *et al.* [2005] investigated multiphase flow processes and
76 quantified drainage paths showing that water is preferentially lost from larger pores and the
77 drainage of the remaining disconnected pores is prevented. Since then Tippkotter *et al.*
78 [2009] detected soil water in macropores and measured water film thickness at a 20 $\mu$m
79 resolution. They quantified the water without the use of contrast enhancing agents or
80 comparison of wet and dry scans. Partial volume effects make separating boundaries between
81 phases of interest a challenging task, due to the material of concern often failing to fully fill a
82 voxel [*Ketcham and Carlson*, 2001]. This can lead to individual voxels being misclassified.
83 However, as a microfocus system with a fine resolution was used in the study, the impact of
84 voxel misclassification is minimised [*Clausnitzer and Hopmans*, 2000]. The most recent
85 advances in CT imaging technology now allow 3D non-destructive imaging of soils at even
86 higher resolutions, *e.g.* <3 $\mu$m spot size [*Zappala et al.*, 2013], allowing water to be observed
87 in smaller pores than previously considered.

88

89 The macroscopic scale flow in saturated and unsaturated porous media are often described
90 using a Darcy's law and Richards' equation [*Hornung*, 1997]. These equations are
91 parameterised by the unsaturated hydraulic conductivity and WRC. From a mathematical
92 perspective Darcy's law can be derived from the underlying Stokes equations using the
93 method of homogenization [*Keller*, 1980]. This approach has been applied to single porosity

94 materials [*Hornung*, 1997; *Keller*, 1980], double porosity materials [*Arbogast and Lehr*,
95 2006; *Panfilov*, 2000], and porous media containing voids or vugs [*Arbogast and Lehr*, 2006;
96 *Daly and Roose*, 2014]. This method is based on the idea that the underlying porous structure
97 is periodic, *i.e.*, it is composed of a set of regular repeating units. By calculating the average
98 fluid velocity for a single representative unit volume due to a unit pressure drop, Darcy's law
99 and the representative hydraulic conductivity can be derived [*Pavliotis and Stuart*, 2008;
100 *Taylor et al.*, 1970]. The mathematics underlying the WRC is less well established and
101 homogenization studies to date have assumed that the air water interface is known in advance
102 [*Taylor et al.*, 1970].

103

104 Image based modelling can be loosely divided into two categories: pore network modelling
105 and direct simulation [*Blunt*, 2001; *Blunt et al.*, 2013]. The first of these, pore network
106 modelling, refers to the extraction of a representative network from the pore scale geometry
107 [*Fatt*, 1956] and has been widely used to predict averaged properties of packed spheres
108 [*Bryant and Blunt,* 1992; *Bryant et al.,* 1993b] and imaged porous media [*Blunt, 2001; Blunt*
109 *et al.,* 2013; *Bryant et al.,* 1993a]. This technique is able to reproduce relative permeability
110 curves and water release characteristics. However, the pore network extraction results in a
111 simplified geometry which may neglect important pore scale phenomena. The alternative
112 technique of direct modelling involves solving equations directly on the imaged geometries.
113 This technique captures the detail of the pore scale geometry down to the resolution limit.
114 The key disadvantage is that modelling multiphase flow is demanding from a computational
115 point of view. Typically models of this type are based on Lattice Boltzman simulations of
116 two fluids as these are highly parallel and relatively easy to implement [*Gao et al.*, 2012;
117 *Ramstad et al.*, 2010]. Other image based modelling studies in porous media include 3D
118 image based simulations of nutrient transport [*Keyes et al.*, 2013] and saturation based flow

119 modelling of water movement in 2-D image slices [*Aravena et al.,* 2014; *Aravena et al.,*
120 2011].

121

122 In this paper we demonstrate the application of a high resolution CT method to quantify
123 water distribution in soil pores under successive reductive drying. Using the structural
124 geometries from the CT images we apply the method of homogenization combined with
125 direct image based modelling to calculate the hydraulic conductivity across a range of matric
126 potentials. This can be seen as analogous to the measurement of a wetting phase relative
127 permeability curve. Specifically the question we aimed to answer is: what is the smallest
128 possible Representative Elementary Volume (REV) required to determine a hydraulic
129 conductivity approximation which is globally valid? In addition the soil moisture content is
130 calculated directly from the CT images at a range of different matric potentials and, hence,
131 the WRC is derived. This approach is chosen, rather than Lattice Boltzmann simulation, as it
132 allows the WRC and hydraulic conductivity to be calculated quickly without the need for
133 time consuming two fluid simulations. From the images we are able to obtain information on
134 soil drainage in both undisturbed field cores and sieved soils. This was used to accurately
135 determine the impact of soil structure on hydraulic behaviour.

136

137 **3. Materials and Methods**

138

139 *3.1. Sample preparation*

140 Soil was obtained from The University of Nottingham farm at Bunny, Nottinghamshire, UK
141 (52.52° N, 1.07° W). The soils used in this study were a Eutric Cambisol (Newport series,

loamy sand/sandy loam) and an Argillic Pelosol (Worcester series, clay loam). Particle size analysis for the two soils was: 83% sand, 13% clay, 4% silt for the Newport series and 36% sand, 33% clay, 31% silt for the Worcester series. Typical organic matter contents were 2.3% for the Newport series and 5.5% for the Worcester series [*Mooney and Morris, 2008*]. From herein the two soil types are referred to as sand and clay soil. Loose soil was collected from each site in sample bags and field cores (10 mm height, 10 mm diameter) were collected from the immediate soil surfaces after any residues had been cleared. Four replicates were collected for each soil type. Saturated hydraulic conductivity measurements of the field cores were obtained via the standard laboratory method using a constant head device [*Rowell*, 1994]. Experimentally obtained hydraulic conductivity measurements were made for comparison with the calculated values.

### *3.2. Measurement of the soil water release characteristic*

In order to investigate the effect of drying on soil water distribution and soil structural changes in 3D, a custom-built tension table was designed to hold the soil sample at a given matric potential, whilst undergoing CT scanning. A small vacuum chamber was constructed (Supplementary Figure 1), that contained a porous ceramic plate (Soil Moisture Corp, Santa Barbara, CA, U.S.A) on top of which a field soil core was placed, with kaolin clay at the base to ensure a good contact. The sample size was kept small to ensure high resolution scanning based on the sample size:resolution trade off that limits CT studies [*Wildenschild et al.*, 2002]. The porous ceramic was first submerged in de-aired deionized water and a vacuum applied to ensure no air bubbles remain trapped within the ceramic. The plastic chamber had an O-ring seal at the base and a flange, which was screwed together to ensure an air-tight fit. All components of the chamber were made from plastic to avoid possible image artefacts,

166 which could result from using high X-ray attenuating construction materials such as metal. A
167 0387 Millipore vacuum pump (Merck Millipore, MA, USA) was attached to the chamber and
168 the soil columns were initially saturated from below with deionized water before being
169 placed under a vacuum of -5 kPa (50.8 mmHg), -10 kPa (76.2 mmHg), -20 kPa (152.4
170 mmHg), -40 kPa (304.8 mmHg), -60 kPa (457.2 mmHg) and -75 kPa (533.4 mmHg). It was
171 not possible to achieve pressures in excess of -75 kPa in the system described. The vacuum
172 pump was enabled for 120 min then the valve sealed to retain the vacuum inside the chamber.
173 At each matric potential the soil core inside the chamber was scanned (further details in next
174 section). After each scan the soil core was removed from the chamber and weighed to
175 calculate gravimetric water content.

176

177 Using a combination of sand tables, pressure plates and pressure membrane apparatus, the
178 WRC were obtained for both soil types. Using conventional methods the van Genuchten
179 model [*van Genuchten*, 1980] was fitted to the data. The sand table was prepared by filling
180 the water reservoir and raising it above the base height of the table to ensure full saturation of
181 the sand table with no air bubbles. Both undisturbed field cores and sieved samples (packed
182 to a bulk density of 1.2 g $cm^{-3}$) were placed flat on the sand table. To obtain the mid-range
183 points on the WRC, a pressure plate Model 1600 Pressure Plate Extractor (Soil Moisture
184 Corp, Santa Barbara, CA, U.S.A) was used. Samples were placed on the plate and the
185 samples were weighed frequently until equilibrating at a series of matric potentials. To obtain
186 measurements at lower matric potentials, a pressure membrane apparatus was used. For the
187 sieved samples the required mass of soil was carefully placed into the metal vessels of the
188 pressure membrane apparatus and saturated with air-free water. The field core samples were
189 directly collected in the metal cores and placed onto the apparatus. The collection tubes were

190 weighed frequently and once equilibrated the system was adjusted to higher pressures. After
191 the final measurement, soil samples were oven dried at 105 °C for 24 hr then weighed.

192

193 The measured volumetric water content of the field structured soil cores ($\theta$), accounted for
194 the likely presence of stones and their overall influence on the WRC [*Gardner*, 1965;
195 *Reinhart*, 1961]. The volumetric water content of the soil is written as $\theta$ which is measured in
196 $\frac{\mathrm{cm}^3(\mathrm{H_2O})}{\mathrm{cm}^3(\mathrm{Soil})}$. To calculate this a correction was applied to the measured volumetric water content
197 of the sample, $\theta_m$, which is measured as $\frac{\mathrm{cm}^3(\mathrm{H_2O})}{\mathrm{cm}^3(\mathrm{Total})}$. This stone correction was calculated
198 using

$$\theta = \theta_m \left(1 + \frac{V_s}{V_f}\right), \tag{1}$$

199 where $V_f$ is the fine soil volume measured in $\mathrm{cm}^3(\mathrm{soil})$ and $V_s$ is the volume of stones which
200 is measured in $\mathrm{cm}^3(\mathrm{stones})$ and calculated by subtracting the soil volume from the total
201 sample volume.

202

203 *3.3. X-ray Computed Tomography and analysis*

204 Four replicates from each soil type of the field cores were scanned at the seven matric
205 potentials giving a total of 56 scans for the field structured cores. As they would not be used
206 for individual pore characterisation analysis only three replicates were scanned for the sieved
207 soils leading to 42 additional scans and a total overall number of 98 scans. The field of view
208 for each scan included the entire sample and each scanned sample created a dataset
209 approximately 25 gigabytes in size, which includes all the associated image stacks for

210 analysis, therefore 2.4 terabytes of data was collected. X-ray CT scanning was performed
211 using a Phoenix Nanotom 180NF (GE Sensing & Inspection Technologies GmbH, Wunstorf,
212 Germany). The scanner consisted of a 180 kV nanofocus X-ray tube fitted with a diamond
213 transmission target and a 5-megapixel (2316 x 2316 pixels, 50 x 50 $\mu$m pixel size) flat panel
214 detector (Hamamatsu Photonics KK, Shizuoka, Japan). A maximum X-ray energy of 100 kV
215 and 140 $\mu$A was used to scan each soil core. A total of 1440 projection images were acquired
216 over a 360° rotation. Each projection was the average of 3 images acquired with a detector
217 exposure time of 1 s. The resulting isotropic voxel edge length was 10.17 $\mu$m and total scan
218 time was 105 minutes per core. Although much faster scan times are possible it was
219 necessary in this instance to use a longer scan time to acquire the highest quality images to
220 aid with the phase separation. Two small aluminium and copper reference objects (< 1 $mm^2$)
221 were attached to the side of the soil core to assist with image calibration and alignment during
222 image analysis. Reconstruction of the projection images to produce 3D volumetric data sets
223 was performed using the software datos|rec (GE Sensing & Inspection Technologies GmbH,
224 Wunstorf, Germany).

225

226 The reconstructed CT volumes were visualised and quantified using VG StudioMAX® 2.2
227 (Volume Graphics GmbH, Heidelberg, Germany). Air, soil and water phases of the scanned
228 volume were segmented separately using a threshold technique based on the greyscale value
229 of each voxel using a calibration tool within VG StudioMax v2.2. This works by selecting
230 specific areas of the scanned volume based on greyscale values, which are a result of (X-ray
231 attenuation) density differences within the sample. Image segmentation is the classification of
232 voxels within a CT volume that share common grayscale values and thus X-ray attenuation.
233 The calibration tool allows the user to sample the greyscale value of a selection of voxels that

correspond to the background (*e.g.* the phase/s not considered, this is usually the background air) and then the process is repeated for voxels that correspond to the material of interest (*e.g.* water, air or soil). Based on the greyscale range we segmented all voxels above a 50% mean value between the background and material of interest and define them as a particular phase (i.e. a region of interest). In a two phase sample air is usually used as the background greyscale value to calibrate against. However, as we required the segmentation of three phases, two vessels, one containing soil pore water and the other finely sieved soil (< 100 $\mu$m) for either the sand or clay soil were securely fitted to the inside of the chamber for each scan. The soil pore water and finely sieved soil remained separate from the soil core, but within the imaging field of view, which was important as the soil core sample can change in overall greyscale range over the course of the experiment due to localised drying and X-ray filament aging. Using this approach these separate vessels were used as reference objects during image analysis. It was important that reference vessels were included in every scan as CT scanning is subject to minor variations in greyscales between scans as the system filament ages. A schematic representation of the water segmentation method is presented in Supplementary Figure 2. The first stage was to create a region of interest (ROI) that included all phases except the air filled pore space. This was done by selecting the air space around the sample as the background, ensuring all voxels except those of air would be included as the material of interest and a 3D ROI was then created and labelled 'Water and soil ROI' *e.g.* air not included. The process was then repeated, but utilising the soil inside the reference vessel as a reference value for the solid material. It was used as a reference as it contained limited water and air, hence this 3D ROI was labelled 'Soil'. Subtraction of the 'Soil ROI' from the 'Water and soil ROI' resulted in a ROI with voxels of grey scale values attributed to 'soil water only', *e.g.* the range of voxels remaining after the soil and air ROIs have been subtracted. The volume of the resulting 'Soil Water' ROI was validated against the water

reference object and traditional methods of determining volumetric water content (weighing). Using this approach we assume all organic matter is classified as 'soil'. To create an ROI that included solely the air filled pore space, the ROI that included all material except the air was inverted using the 'Invert ROI' function in VG StudioMax software. The volume analyser tool in VG StudioMax was subsequently used to quantify the total volume of the air and water filled pores. Reconstructed volumes for each matric potential were aligned in VG StudioMax using the metal reference objects on the outside of the sample container. After segmentation of the soil core volumes, a cylindrical ROI shape template was used to subtract the surrounding column and air space from the volume to remove the cylinder of soil. This template was used to ensure the same volume was used for each sample before analysis. No significant evidence of shrinkage was observed across the range of low matric potentials considered here. We note that when three phases (air water and soil) are present in an image erroneous films of the intermediate phase can often be segmented out between the high and low density phases. In this case erroneous films of water could be introduced through segmentation. However, as thin water films only contribute a total flow proportional to the third power of the film thickness these are not a concern in this study.

Image stacks of the extracted volumes were exported and subsequently analysed for individual water filled and air filled pore characteristics for the field structured soil only using ImageJ v1.42 (http://rsbweb.nih.gov/ij/) [*Ferreira and Rasband*, 2011]. For 2D analysis objects less than two pixels (twice the resolution) in diameter (0.02 mm) and for 3D analysis objects less than two voxels in each direction ($8 \times 10^{-6}$ $mm^3$) were regarded as potential noise as a precaution [*Wildenschild et al.*, 2005] and subsequently excluded from the analysis. The BoneJ plugin algorithm [*Doube et al.*, 2010] (http://bonej.org/) in ImageJ software was used to measure discrete individual 3D water filled and air filled pore characteristics namely

284 volume, surface area and thickness (diameter). A voxel is classed as connected to another
285 voxel if it at least touches corner to corner. ImageJ was used to measure the 2D pore shape
286 characteristic 'circularity', which is a measure of an object's similarity to a circle. A value of
287 1 describes a perfect circle and as the value decreases, the object becomes increasingly
288 elongated. The circularity was determined using

289 $$C = \frac{4\pi(A_p)}{(P_p)^2}, \quad (2)$$

290 where $A_p$ is the pore area and $P_p$ is the pore perimeter. The water-filled pore image stack was
291 skeletonised and from this the 3D connectivity (the sum of all the thin (1 voxel) pathways
292 that still preserve the connected topology and original shape of the object) of the water-filled
293 pore volume was also calculated.

294

295 In order for the geometries of the water-filled pores to be modelled, surface mesh files (.stl)
296 were required which were generated in VG StudioMax v2.2. After segmentation of the soil
297 water phase, a cube shaped ROI template was imported to create identical cubes for the
298 surface mesh generation. Each sample was subsampled, from random initial coordinates, with
299 6 cubes comprising side lengths of 3.8 mm. The same coordinates were used for different
300 matric potentials of the same sample. Each individual surface mesh file took between 0.5 – 2
301 hours to generate depending on the complexity of the surface.

302

303 *3.4. Modelling*

304 The hydraulic conductivity of the soil was calculated using the method of homogenization
305 [*Pavliotis and Stuart*, 2008]. This method allows an average Darcy's law to be defined
306 which is applicable to the soil column and is parameterised by the pore scale geometry of the

307 soil. The key assumption used was that the hydraulic properties of the soil can be accurately
308 captured by studying a small subsample of the soil [*Fowler*, 1997], this is often referred to as
309 the Representative Elementary Volume (REV). In this paper we were particularly interested
310 in determining the minimum size REV for which the calculated hydraulic conductivity
311 converges to the macroscopic hydraulic conductivity for soil samples of the order of a few
312 millimetres. This method allowed us to theoretically determine the required sample size for
313 CT analysis of water flow in soil at this scale.

314

315 We note that the averaged hydraulic conductivity and WRC calculated at this scale are not
316 globally applicable. Rather they describe the average flow rate in soil of this type assuming
317 no large scale features such as cracks or larger voids are encountered. In theory these features
318 could be included by deriving an averaged Darcy's law for each soil type, Stokes' equations
319 for large void spaces and approximate Darcy's laws for fractures equation [*Hornung*, 1997].
320 These systems could, in principle, be upscaled to derive averaged Darcy's laws on a much
321 larger scale. However, in this paper our focus is in obtaining an estimate of the hydraulic
322 properties of soils based on their pore structure. Hence, we neglect these larger scale features
323 but emphasise that they could be included through an additional level of upscaling.

324

325 As we are able to segment the air and water separately from the CT images, the fluid
326 dynamics can be greatly simplified. Rather than focusing on the moving interface between
327 each phase, we consider the relatively slow, flow of water about a fixed interface. The
328 resulting equations are introduced in the appendix. We further simplify the equations by
329 assuming that the non-wetting phase, in this case air, is stationary. This assumption is valid
330 assuming that the air phase is disconnected. If this is not the case then the movement of the

331 air effectively lubricates the movement of water resulting in an increase in the hydraulic
332 conductivity. This approach is valid assuming that the pressure gradients are sufficiently
333 low, such that the interface remains fixed, and that the non-wetting phase is not connected,
334 hence, the trapped non-wetting phase has zero average velocity.

335

336 Strictly speaking the theory of homogenization requires the soil structure to be periodic.
337 Clearly for real soil samples this is not the case. This is overcome by enforcing an apparent
338 image based periodicity either by translation or reflection of the CT image (Figure 1). In this
339 paper reflection was chosen as it simplifies the resulting calculations and does not introduce
340 discontinuities in the soil structure. The error induced by enforcing periodicity is that the
341 geometry considered numerically is now fully periodic rather than quazi-periodic and does
342 not truly represent the imaged soil structure. To overcome this, different size REVs were
343 taken from the segmented .stl files, see Figure 1. Specifically, the 6 cubes which were
344 segmented from each scan were of the same volume $V_m = 54.9\ \mathrm{mm}^3$, and were assumed to
345 be sufficiently large that the soil properties would have converged. The REVs sampled from
346 the six cubes were of volume $V = V_m/(2^j)$, where $j$ is a positive integer in the range 0 to 10
347 such that the smallest volume we consider is $0.053\ \mathrm{mm}^3$ and the largest is $V_m$. As $j$ is
348 decreased and, hence, the size of the REV is increased, the relative size of the errors induced
349 by the reflection decreases. Similarly as the REV size increases, the hydraulic properties of
350 the subsample will, in principle, converge to the hydraulic properties of the soil.

351

352 A rigorous analysis of equations governing fluid flow through soil is given in [*Daly and*
353 *Roose*, 2014]. Here we provide a brief description of the theory in the applied context with
354 further details given in the appendix. We consider a sample of soil which is large with respect

355 to the REV size. Specifically if the REV is a small cube with side length $L_y$ and the large
356 sample we are interested in has characteristic length $L_x$ then we require that the ratio of these
357 two lengths is small, *i.e.*, $\epsilon = L_y/L_x \ll 1$. For typical pore sizes observed in soil, the
358 viscous forces dominate [*Fowler*, 1997]. Hence, we may consider the Stokes limit of the
359 Navier-Stokes equations where all inertial terms are neglected. Mathematically the
360 macroscopic hydraulic conductivity, which is valid for the whole soil column, is obtained in
361 two steps. First, it is shown, see appendix for details, that pressure variations across the REV
362 of size $\epsilon$ will induce a water velocity also of size $\epsilon$. Secondly, a set of equations are derived
363 which allow the pressure driven fluid velocity to be determined based on the soil (Figure 1).
364 Finally, the average velocity over the REV is used to determine a Darcy's law which is
365 independent of $\epsilon$. This value is valid for the bulk soil and describes fluid driven by an
366 external pressure gradient, see [*Daly and Roose*, 2014]

$$\boldsymbol{u} = -\mathcal{K}(\boldsymbol{\nabla} p_0 - \rho g \hat{\boldsymbol{e}}_z), \tag{3}$$

367 where $\rho$ is the fluid density ($\rho = 10^3 \mathrm{kg\,m^{-3}}$ in the case of water), $g = 9.8\ \mathrm{m\,s^{-2}}$ is the
368 acceleration due to gravity, $p_0$ is the applied pressure, $\boldsymbol{u}$ is the volume averaged water
369 velocity and $\mathcal{K}$ is the relative permeability (in the general case a tensor) which has
370 components defined as

$$\mathcal{K}_{jk} = \frac{L_y^2}{\mu} \int_{\Omega_w} \hat{\boldsymbol{e}}_j \cdot \boldsymbol{v}_k^w \, dy. \tag{4}$$

371 Here $\hat{\boldsymbol{e}}_j$, for $j = x, y, z$ is a unit vector in the $j$-th direction and $\boldsymbol{v}_k^w$ is the local velocity.
372 Assuming that the air velocity is slower than the water velocity then $\boldsymbol{v}_k^w$ satisfies the cell
373 problem

$$\boldsymbol{\nabla} \cdot \sigma_k^w - \boldsymbol{\nabla}\pi_k^w = \hat{\boldsymbol{e}}_k, \qquad \boldsymbol{x} \in \Omega_w, \quad (5a)$$

$$\boldsymbol{\nabla} \cdot \boldsymbol{v}_k^w = 0, \qquad \boldsymbol{x} \in \Omega_w, \quad (5b)$$

$$\boldsymbol{v}_k^w = 0, \qquad \boldsymbol{x} \in \Gamma_s, \quad (5c)$$

$$\boldsymbol{v}_k^w = 0, \qquad \boldsymbol{x} \in \Gamma_{aw}, \quad (5d)$$

where $\sigma_k^w = (\boldsymbol{\nabla}\boldsymbol{v}_k^w) + (\boldsymbol{\nabla}\boldsymbol{v}_k^w)^T$, $\pi_k^w$ is the local pressure correction due to the microscale geometry, the superscript $w$ denotes the water phase, $\Omega_w$, $\Gamma_s$ and $\Gamma_{\mathrm{aw}}$ denote the water domain, the soil boundary and the air-water interface respectively. Physically this can be thought of as calculating the fluid velocity subject to a unit pressure gradient. As the equations are linear Darcy's law follows by multiplying the result by the desired pressure gradient.

Equations (5) were solved numerically on each subsample obtained from the CT images using OpenFOAM, an open source Computational Fluid Dynamics toolbox running on IRIDIS, the High Performance Computing Facility at the University of Southampton. The hydraulic conductivity is then calculated as the average water velocity due to gravity. Results were obtained for each soil sample using the method illustrated in Figure 1. The 6 cube surface meshes, generated from each soil core, were repeatedly sampled to obtain 3D REVs of increasing size. The result is a set of hydraulic conductivity calculations which we expect to converge to the true hydraulic conductivity of the soil, at each point along the WRC, as the sub-volume size is increased.

### *3.5. Statistical analysis*

392 The results obtained directly from the CT images were analysed by general analysis of
393 variance (ANOVA) containing soil type and matric potential and all possible interactions
394 as explanatory variables using Genstat 15.1 (VSN International, UK).

395

396 **4. Results & Discussion**

397

398 *4.1 Hydraulic properties*

399

400 The clay soil contained an average stone volume of 0.2 $cm^3$ whereas the average stone
401 volume for the sand soil was 5.5 $cm^3$ (total soil volume was 55 $cm^3$). Therefore although field
402 structured soil was able to retain water for longer, as shown by the curves from the
403 conventional method (Figure 2), the influence of stones was not a consideration and the
404 greater water holding capacity is attributed to the more complex pore network in the field
405 structured soil.

406

407 There are clear differences between sieved soil and field structured soil (Figures 2 and 3). For
408 the field structured soil the imaging technique shows a good agreement with the conventional
409 methods with an average error of < 5% across the range of matric potentials considered. The
410 sieved soil responded more strongly to pressure change in comparison to the field structured
411 soil. However, the imaged sieved soil data did not show this trend, hence, there was quite a
412 large error of 9% at 0 kPa and as high as 65% at -75 kPa. This suggests that, for the field

413 structured samples, the segmentation procedure was successful at identifying the majority of
414 the water filled pores (WFPs).

415

416 It is somewhat surprising that the more homogeneous sieved soil is less well represented
417 through the imaging technique than the field structured soil. However, we attribute this to the
418 pore size distribution in the two soils. The field structured soil has a wider range of pore
419 sizes than the sieved soil which contains macropores defined by the largest grain size. As the
420 matric potential becomes increasingly negative, the water drains from smaller and smaller
421 pores. In the case of the field structured soil this results in a gradual decrease in volumetric
422 water content with matric potential which the imaging technique can follow assuming the
423 pore size is larger than the image resolution. In the case of the sieved soil there is a reduced
424 range of pore sizes and the water quickly drains from the larger pores and remains trapped in
425 a large number of smaller pores. The result is that the volumetric water content drops quickly
426 as the matric potential is reduced and the imaging technique, which cannot resolve the
427 smallest pores, fails to capture this. We also note that the differences observed in the WRC
428 between the two soil types is smaller when measured using the imaging technique than using
429 conventional methods. This is again attributed to the finite resolution of the measurements
430 and is analogous to the increasing error observed as the saturation is decreased.

431

432

433 The hydraulic conductivity, which corresponds to the water release curves shown in Figure 2,
434 has been calculated by solving equations (5) for increasing subsample size. As the subsample
435 size was increased, the hydraulic conductivity converged to a fixed value which we interpret

436 as the macroscopic hydraulic conductivity (Figure 4). The sample size at which this occurred
437 was smaller for lower matric potentials. This is attributed to the increased air-filled porosity
438 which decreases the contact area between the water and the soil. Hence, the effect of the
439 heterogeneous soil boundary is decreased and the overall homogeneity of the sample is
440 increased. We note that, as convergence is seen to occur at smaller sample sizes for lower
441 saturation, fewer simulations were run at these saturation values. This occurs at
442 approximately ¼ of the sample volume for all matric potentials for both soils. We note that
443 although the REV volume is approximately the same for all soil types considered, the
444 properties obtained from this analysis are different for different soil types. This method
445 therefore enabled the required sample size for CT analysis of water flow in these samples to
446 be determined, which was a cube volume of 11 $mm^3$. This sample was large enough for
447 convergence of the calculated hydraulic conductivity, meaning that the sample size contained
448 an adequate volume of soil to capture the averaged hydraulic properties on this scale.
449 Therefore considering the averaging method used in this paper, the hydraulic conductivity is
450 globally valid. This means that the representative volume of 11 $mm^3$ is an appropriate
451 representative volume element for the global hydraulic conductivity of the soil samples used
452 in this study. However, there may be significant features, such as cracks or heterogeneities in
453 the soil, which are not captured in the 11 $mm^3$ volume. Hence, care must be taken in
454 applying these results on the field scale and an additional level of upscaling may be required
455 to capture the properties of these features.

456

457 The method described in Section 3.4 and the appendix allowed us to also obtain the hydraulic
458 conductivity in unsaturated soils as well as in $x$, $y$ and $z$ directions. It was expected the flow
459 would be dominant in the $z$ direction due to gravity, however (possibly due to the size of the
460 samples) we did not observe this. The calculated hydraulic conductivities are shown as a

function of matric potential in Figure 5. The calculated hydraulic conductivities and the corresponding WRC have been fitted to the van Genuchten model for the WRC and the unsaturated hydraulic conductivity [*van Genuchten*, 1980] using a non-linear least squares method. We note that we have only done this fitting for the imaged data as we do not have hydraulic conductivity measurements for the full range of matrix potentials using conventional measurements. The volumetric water content $\theta$ is given by

$$\theta = (\theta_s - \theta_r)\left(\frac{1}{1+(\alpha h)^n}\right)^m + \theta_r, \tag{6}$$

where $\theta_s$ and $\theta_r$ are the saturated and residual volumetric water content respectively, $h$ is the is the matric head, $m = 1 - 1/n$ and $n$ and $\alpha$ are the van Genuchten parameters. The corresponding hydraulic conductivity is given by $K = K_{sat}k_r^{vg}$. Here $K_{sat}$ is the saturated hydraulic conductivity and the relative hydraulic conductivity is given by

$$k_r^{vg} = \frac{\{1-(\alpha h)^{n-1}[1+(\alpha h)^n]^{-m}\}^2}{[1+(\alpha h)^n]^{m/2}}. \tag{7}$$

We take $\theta_r$ to be negligible and fit the remaining parameters to the imaged data. The average saturated hydraulic conductivity and the fitted parameters: $K_{sat}$, $\theta_s$, $\alpha$ and $n$ are shown in Table 1. The fitted hydraulic conductivity and WRC, obtained using these parameters, are shown in Figure 5.

**Table 1. Fitted van Genuchten parameters**

| **Soil** | **Measured $K_{sat}$ $[cm\ s^{-1}]$** | **Calculated $K_{sat}$ $[cm\ s^{-1}]$** | **Saturated volumetric water content $\theta_s$** | **$\alpha$ $[cm^{-1}]$** | **$n$** |
|---|---|---|---|---|---|
| Sand | 0.0013 | 0.0014 | 0.418 | 0.153 | 1.71 |
| Clay | 0.0004 | 0.0010 | 0.423 | 0.148 | 1.66 |

477 The hydraulic conductivity decreases as the matric potential decreases from 0 kPa to -75kPa
478 ($P<0.001$) and is slightly larger in the sand soil compared to the clay soil. The van
479 Genuchten model fits the imaged data well with a slight discrepancy in the WRC at 0 kPa
480 (RMSE=0.016 for the clay soil and RMSE=0.022 for the clay soil). The experimentally
481 measured hydraulic conductivity agreed well with the calculated value for the sand soil.
482 However, the data compares less favourably in the case of the clay soil where the
483 experimentally measured hydraulic conductivity is less than half that of the calculated value.

484

485 The differences observed for the clay soil between the experimentally measured hydraulic
486 conductivity and the calculated values are attributed to a combination of image resolution and
487 segmentation limitations. Typically clay soils have much smaller pores than sand soils, due
488 to the differences in particle size and as such will have a large number of pores which are
489 comparable with or below the imaging resolution used in this study. Further complications
490 include partial volume effects, which can cause errors in voxel classification, if the boundary
491 is between two phases with wide ranging attenuation values, such as air and rock [*Ketcham*
492 *and Carlson*, 2001]. This therefore could lead to an incorrect classification of voxels resulting
493 in either an overestimate or an underestimate of the pore space and pore size distribution due
494 to the effect it has on objects of differing sizes which may explain why we have an
495 overestimation at the wet end, and underestimation at the dry end. As the calculated
496 hydraulic conductivity is large with respect to the measured value we expect that the pore
497 space is being over estimated in this case.

498

499 *4.2 Pore characteristics*

500 In order to obtain a better understanding of the pore scale processes which contribute to the
501 macroscopic hydraulic properties we consider the distribution of air and water within the soil
502 matrix on the pore scale. In order to quantify the air and water content we define Air Filled
503 Pores (AFPs) and Water Filled Pores (WFPs) as single connected regions of air or water
504 respectively. We also define the pore space as the union of all the AFPs and WFPs.
505 Throughout this paper when discussing connected regions of water and air we exclusively use
506 this terminology in keeping with the soil science literature. In addition we refer to individual
507 pores within the soil to define simply connected pathways between two distinct points within
508 the pore space. Typically, the pore space contains a single large WFP which contains over
509 50% of the water within the pore space and a large number of much smaller AFPs and WFPs.
510 The connected WFPs are the main contributor to both the WRC and the hydraulic
511 conductivity calculations. However, insight may be gained into the wetting and drying
512 behaviour of the soils by considering the properties of the AFPs. It is possible to determine
513 the interfacial area between water and air phases [*Costanza-Robinson et al.*, 2008]. However,
514 as previous studies have made the calculations based on porous media other than soil, this is
515 not comparable to the work undertaken in this study. In addition the majority of the previous
516 work in soil [*Falconer et al.*, 2012; *García-Marco et al.*, 2014; *Tucker*, 2014], refer directly
517 to WFPs and AFPs as such it is more meaningful in the context of the literature to consider
518 the WFP and AFP surface area.

519

520 At 0 kPa we have a residual AFP volume of approximately 6% of the total pore space, see
521 supplementary Figure 3. This volume corresponds to trapped air pockets which, due to the
522 high tortuosity of the soil structure, remain in the pore space at saturation. As the matric
523 potential is made more negative, the total WFP volume decreases and the corresponding AFP
524 volume increases (Figure 6; $P<0.001$). In addition to the change in WFP and AFP volume,

525 the total soil volume is seen to increase by up to 10%. Whilst this may, in part, be attributed
526 to segmentation issues and partial volume effects, it is also likely that changes in soil
527 structure are responsible for this apparent increase. The total AFP volume and the
528 corresponding AFP surface area did not vary significantly across the different soil types (sand
529 and clay). However, the average volume and the corresponding surface area of an individual
530 AFP averaged across all matric potentials shows significant variation across soil types
531 ($P<0.001$) with average AFP volume of $0.00115\ mm^3$ in the clay soil compared with
532 $0.00163\ mm^3$ in the sand soil and with average AFP surface area of $0.0109\ mm^2$ in the clay
533 soil and $0.0182\ mm^2$ in the sand soil. This greater surface area corresponds to a much
534 greater number of AFPs at -75 kPa in the clay soil (104 pores/$mm^3$) than the sand soil (55
535 pores/ $mm^3$), ($P<0.05$). The average pore thickness decreased significantly with decreasing
536 matric potential (Figure 7; $P<0.001$), from an average of 0.030 mm at 0 kPa to 0.026 mm at -
537 75 kPa. There was no significant difference between soil types. At 0 kPa the average pore
538 thickness for the clay soil was 0.027 mm compared to 0.033 mm for sand. At -75 kPa the
539 average pore thickness for the clay and the sand soils was just 0.026 mm.

540

541 To highlight the differences in the soil types we classify the AFPs as air filled macro (> 100
542 $\mu$m), air filled meso (30 - 100 $\mu$m) and air filled micropores (21 – 30 $\mu$m), see supplementary
543 Figure 4. This classification is based on the pore diameter, *i.e.* the maximum sphere diameter
544 which can fit inside the pore. The air filled micropore range is limited by the achievable
545 resolution based on our estimation of image noise (> 2 voxels). As the matric potential is
546 decreased, the total number of AFPs classified into each category changes with an overall
547 increase in the number of air filled macropores seen in the case of the sand soil. In the sand
548 soil there is a linear increase in the percentage of air filled macropores with soil drainage, this

549 was expected due to the high number of macropores throughout the sand structure, which is
550 typically more homogenous compared to the clay. The clay soil had a less regular drainage
551 pattern than the sand soil. There is a linear increase in the air filled micropore percentage as
552 the clay dried. However, the percentage of air filled macropores is quite irregular and can be
553 attributed to the occurrence of crack formation which is more likely in clay soil. The average
554 pore circularity of the AFPs, equation (2), also increased as matric potential decreased. At -75
555 kPa the AFP space was comprised of pores with an average circularity of 0.78 compared to a
556 circularity value of 0.72 at 0 kPa ($P<0.001$). Our results also show that at drier matric
557 potentials the shape of the air and water filled pores become increasingly rounded possibly
558 linked to air bubble-style pore formation. This measurement enables us to quantify the
559 influence of pore shape on soil drainage. However we note this is only a single measure and
560 further descriptors that account for the shape of the soil porous architecture in 3D are
561 required to advance understanding in this area. The 3D connectivity of the WFPs decreased
562 with decreasing matric potential ($P<0.05$), pore connectivity was significantly greater in the
563 clay soil at all matric potentials ($P<0.01$). The differences in the AFP structure in the two
564 soil types are indicative of the soil structure. The clay soil contains a large number of micro-
565 pores which corresponds to the large number of air filled micropores trapped within the soil
566 structure. In contrast the sand soil contains a larger number of meso- and macro-pores
567 causing the air to be contained in relatively few, larger volumes. It is highly likely that the
568 clay soil contained many pores that were too small to be imaged at the achievable resolution
569 in this study.

570

571 **5. Conclusions**

572

573 In this paper we have used a combination of CT imaging and mathematical modelling to
574 derive the WRC and unsaturated hydraulic conductivity in contrasting soil textures (*i.e.* clay
575 and sand) and structures (i.*e.* sieved and field structured soil). The ability to non-
576 destructively scan the soil cores and segment the water and air filled pores from the soil
577 matrix combined with the mathematical modelling have provided a unique insight into the
578 WRC and hydraulic properties of contrasting soils. A comprehensive study of the hydraulic
579 properties of different soil types based on a quantitative visual assessment of the soil structure
580 has been carried out across a range of different saturation values. The results predict the
581 increase in hydraulic conductivity with saturation and highlight the structural basis for the
582 differences between sand and clay soils.

583

584 The data obtained via CT imaging allows us to visualise the soil structure in 3D and, hence,
585 to measure the effects of pore geometry on the WRC. Using the scanned geometry combined
586 with detailed mathematical modelling, the unsaturated hydraulic conductivity and, hence,
587 hydraulic conductivities were obtained at the precise measured matric potentials. These
588 values are not easily measured in the laboratory through experimentation alone. Using the
589 measured saturated hydraulic conductivity and typical soil parameters we have compared the
590 computed values against the van Genuchten model. The simulated values compared well with
591 the measured saturated hydraulic conductivity values. The calculated hydraulic properties of
592 the clay soil against the van Genuchten model compare well. However, in the case of the
593 sand soil, the calculated values are lower than those obtained using the van Genuchten model.
594 This highlights the potential structural differences between two soils of a particular textural
595 class and the potential role played by the micro-porous structure of the aggregates which are
596 currently below the imaging resolution of CT for this sample size.

The combination of CT imaging and modelling provides a new level of understanding of the role that structure plays in the averaged properties of soil. The WRC has been obtained via CT imaging and provides a detailed geometric representation of how the water is retained in pores of different sizes. A downside to the imaging approach is the time investment required to collect the data. However, this is comparable to the conventional laboratory method as the majority of time is spent allowing the sample to equilibrate. However, this detailed information on the pore-scale architecture represents a significant development in our ability to study soil systems which will continue to advance pore scale modelling by providing three dimensional geometries against which the numerical models can be tested [19].

## 6. Acknowledgements

The authors acknowledge the use of the IRIDIS High Performance Computing Facility, and associated support services at the University of Southampton, in the completion of this work. This project was funded by BBSRC BB/J000868/1, a collaborative project between Southampton and Nottingham, PI and overall lead Roose. All reconstructed scan data will be available on request by emailing microct@nottingham.ac.uk. The authors extend their thanks to the anonymous reviewers for constructive feedback on their manuscript.

**Table A1. Values of parameters used in numerical calculations**

| Constant | Value | Units | Description |
|---|---|---|---|
| $\rho^w$ | $10^3$ | kg m$^{-3}$ | Density of water |
| $\rho^a$ | 1.2 | kg m$^{-3}$ | Density of air |
| $\mu^w$ | $10^{-3}$ | kg m$^{-1}$ s$^{-}$ | Viscosity of water |
| $\mu^a$ | $20\times10^{-6}$ | kg m$^{-1}$ s$^{-}$ | Viscosity of air |
| $\tilde{g}$ | 9.8 | m s$^{-2}$ | Acceleration due to gravity |
| $r_y$ | $100\times10^{-6}$ | m | Typical pore radius |
| $L_y$ | $10^{-3}$ | m | Typical size of microscale geometry |
| $L_x$ | $10^{-1}$ | m | Typical size of macroscale geometry |
| $\tilde{\gamma}$ | $7.28\times10^{-2}$ | kg s$^{-2}$ | Surface tension |
| $\tilde{\kappa}$ | $10^4$ | m$^{-1}$ | Curvature |
| $\epsilon$ | $10^{-2}$ | | Ratio of geometry sizes |
| $\kappa$ | $2.97\times10^2$ | | Scaled surface tension-curvature product |
| $\lvert\boldsymbol{g}\rvert$ | 1 | | Scaled gravitational force |
| $\delta_u$ | 0.16 | | Typical velocity ratio |
| $\delta_p$ | 8.33 | | Typical pressure ratio |

***Appendix***

The starting point is the non-dimensional Stokes equations using the scaling given in [*Daly and Roose*, 2014]. The dimensional variables, denoted with a $\tilde{\cdot}$, are scaled using

$$\boldsymbol{v}^w = \frac{4\mu^w}{\rho^w \tilde{g} r_y^2}\,\tilde{\boldsymbol{v}}^w, \qquad p^w = \left(\frac{L_x}{L_y}\right)\frac{4L_y}{\rho^w \tilde{g} r_y^2}\,\tilde{p}^w,$$

$$\boldsymbol{v}^a = \left(\frac{L_x}{L_y}\right)\frac{4\mu^a}{\rho^a \tilde{g} r_y^2}\,\tilde{\boldsymbol{v}}^a, \qquad p^a = \left(\frac{L_x}{L_y}\right)^2\frac{4L_y}{\rho^a \tilde{g} r_y^2}\,\tilde{p}^a,$$

$$t = \left(\frac{L_x}{L_y}\right)\frac{\rho^w r_y^2\,\tilde{g}}{4\mu^w L_y}\,\tilde{t},$$

where $\boldsymbol{v}^w$ and $\boldsymbol{v}^a$ are the water and air velocities, $p^w$ and $p^a$ are the water and air pressures, $t$ is the dimensionless time and the remaining parameters are listed in table A1 and the non-dimensional constants are

| | | | |
|---|---|---|---|
| $\kappa = \left(\frac{L_y}{L_x}\right)\frac{4L_y\,\tilde{\gamma}}{\rho^w r_y^2\,\tilde{g}}\tilde{\kappa},$ | $\boldsymbol{g} = \frac{\hat{\boldsymbol{e}}_x L_y^3}{r_y^2 L_x},$ | $\delta_u = \left(\frac{L_y}{L_x}\right)\frac{\rho^w \mu^a}{\rho^a \mu^w},$ | $\delta_p = \left(\frac{L_y}{L_x}\right)\frac{\rho^w}{\rho^a},$ |

Typical values for the non-dimensional numbers are given in table A1. The resulting non-dimensional Stokes equations are:

$$\epsilon \boldsymbol{\nabla} \cdot \sigma^w - \boldsymbol{\nabla} p^w = \epsilon \boldsymbol{g} \qquad \boldsymbol{x} \in \Omega_w, \qquad \text{(A1a)}$$

$$\epsilon \boldsymbol{\nabla} \cdot \sigma^a - \boldsymbol{\nabla} p^a = \epsilon^2 \boldsymbol{g} \qquad \boldsymbol{x} \in \Omega_a, \qquad \text{(A1b)}$$

$$\epsilon \phi \frac{\partial S^w}{\partial t} + \boldsymbol{\nabla} \cdot \boldsymbol{v}^w = 0, \qquad \boldsymbol{x} \in \Omega_w, \qquad \text{(A1c)}$$

$$\epsilon \phi \frac{\partial S^a}{\partial t} + \delta_u \boldsymbol{\nabla} \cdot \boldsymbol{v}^a = 0, \qquad \boldsymbol{x} \in \Omega_a, \qquad \text{(A1d)}$$

$$\boldsymbol{v}^w = 0, \qquad \boldsymbol{v}^a = 0, \qquad \boldsymbol{x} \in \Gamma_s, \qquad \text{(A1e)}$$

$$\hat{\boldsymbol{n}} \cdot \boldsymbol{v}^w = 0, \qquad \hat{\boldsymbol{n}} \cdot \boldsymbol{v}^a = 0, \qquad \boldsymbol{x} \in \Gamma_{aw}, \qquad \text{(A1f)}$$

$$\hat{\boldsymbol{\tau}} \cdot [\boldsymbol{v}^w - \delta_u \boldsymbol{v}^a] = 0, \qquad \boldsymbol{x} \in \Gamma_{aw}, \qquad \text{(A1g)}$$

$$\hat{\boldsymbol{n}} \cdot \left[ (\epsilon \sigma^w - I p^w) - \delta_p (\epsilon \sigma^a - I p^a) \right] = \hat{\boldsymbol{n}} \kappa, \qquad \boldsymbol{x} \in \Gamma_{aw}, \qquad \text{(A1h)}$$

combined with periodic boundary conditions in the x y and z directions. To simplify the problem we notice that $\delta_u^{-1} < 1$ and $\delta_p < 1$ and, therefore, they can be neglected to first approximation. The result is that the air and water velocities decouple we need only consider the flow of water through the soil. The air velocity could in principle be calculated as a perturbation of order $\delta_u$ which in turn would create a water velocity perturbation of order $\delta_u/\delta_p$. However, we expect that this perturbation will be small with respect to the uncertainty in the segmentation and the temperature dependent variations of the water viscosity. The simplified equations are:

$$\epsilon \nabla^2 \boldsymbol{v}^w - \boldsymbol{\nabla} p^w = \epsilon \boldsymbol{g} \qquad x \in \Omega_w, \qquad \text{(A2a)}$$

$$\boldsymbol{\nabla} \cdot \boldsymbol{v}^w = 0, \qquad x \in \Omega_w, \qquad \text{(A2e)}$$

$$\boldsymbol{v}^w = 0, \qquad x \in \Gamma_s, \qquad \text{(A2f)}$$

$$\boldsymbol{v}^w = 0, \qquad x \in \Gamma_{aw}, \qquad \text{(A2g)}$$

We expand the gradient operator $\boldsymbol{\nabla} = \epsilon \boldsymbol{\nabla}_x + \boldsymbol{\nabla}_y$ and look for a power series solution to equations (A4) of the form

$$\boldsymbol{v}^w = \boldsymbol{v}_0^w + \epsilon \boldsymbol{v}_1^w + O(\epsilon^2) \qquad \text{(A3a)}$$

$$p^w = p_0^w + \epsilon p_1^w + O(\epsilon^2) \qquad \text{(A3b)}$$

Substituting equations (A3) into equations (A2) and retaining terms $O(\epsilon^0)$ we obtain $\boldsymbol{\nabla}_y p_0^w = 0$, *i.e.*, the largest component of the pressure is constant over the microscale. Expanding to $O(\epsilon^1)$ we effectively convert the leading order pressure drop into a body force and obtain

$$\boldsymbol{v}_0^w = \sum_{k=1}^{3} \boldsymbol{\nu}_k \partial_{x_k} p_0^w$$

Where $\boldsymbol{\nu}_k$ satisfy the cell problem

$$\nabla_y^2 \boldsymbol{v}_k - \boldsymbol{\nabla}_y \pi_k^w = \hat{\boldsymbol{e}}_k, \qquad \boldsymbol{x} \in \Omega_w, \quad \text{(A4a)}$$

$$\boldsymbol{\nabla}_{\boldsymbol{y}} \cdot \boldsymbol{v}_k = 0, \qquad \boldsymbol{x} \in \Omega_w, \quad \text{(A4b)}$$

$$\boldsymbol{v}_k = 0, \qquad \boldsymbol{x} \in \Gamma_s, \quad \text{(A4c)}$$

$$\boldsymbol{v}_k = 0, \qquad \boldsymbol{x} \in \Gamma_{aw}, \quad \text{(A4d)}$$

$$\boldsymbol{v}_k, \pi_k^w \text{ periodic with period 1} \quad \text{(A4e)}$$

Averaging the velocity over the unit cell we obtain the non-dimensional form of Darcy's law for the average velocity

$$\boldsymbol{u}_0^w = \int_\Omega \boldsymbol{v}_k \otimes \hat{\boldsymbol{e}}_k \, dy \, (\boldsymbol{\nabla}_{\mathrm{x}} p_0^w + \boldsymbol{g})$$

which in dimensional form is equation (3) and (4) in the main paper.

As discussed in the main text we impose periodicity via reflection of the geometry about the x, y and z axis. The result is that the velocity is, for the $k$-th cell problem, the pressure correction $\pi_k^w$ is even odd in the direction $x_k$ and even in the direction $x_j$ for $j \neq k$. Similarly we find that the $k$-th component of the velocity, $\hat{\boldsymbol{e}}_k \cdot \boldsymbol{v}_k$ is even in all directions. The remaining velocity components, $\hat{\boldsymbol{e}}_j \cdot \boldsymbol{v}_k$ for $j \neq k$, are odd in the directions $x_k$ and $x_j$, however, they are even in the direction $x_p$ for $p \neq k$ and $p \neq j$. Specifically the resulting boundary equations and boundary conditions are:

$$\nabla_y^2 \boldsymbol{v}_k - \boldsymbol{\nabla}_y \pi_k^w = \hat{\boldsymbol{e}}_k, \qquad \boldsymbol{x} \in \Omega_w, \quad \text{(A5a)}$$

$$\boldsymbol{\nabla}_{\boldsymbol{y}} \cdot \boldsymbol{v}_k = 0, \qquad \boldsymbol{x} \in \Omega_w, \quad \text{(A5b)}$$

$$\boldsymbol{v}_k = 0, \qquad \boldsymbol{x} \in \Gamma_s, \quad \text{(A5c)}$$

$$\boldsymbol{v}_k = 0, \qquad \boldsymbol{x} \in \Gamma_{aw}, \quad \text{(A5d)}$$

$$\pi_k^w = 0, \ \frac{\partial}{\partial x_k}(\hat{\boldsymbol{e}}_k \cdot \boldsymbol{v}_k) = 0, \ \hat{\boldsymbol{e}}_j \cdot \boldsymbol{v}_k = 0, \ j \neq k \qquad \boldsymbol{x} \in \partial x_k \quad \text{(A5e)}$$

$$\frac{\partial}{\partial x_j}\pi_k^w = 0, \ \frac{\partial}{\partial x_p}\left(\hat{\boldsymbol{e}}_p \cdot \boldsymbol{v}_k\right) = 0, \ \hat{\boldsymbol{e}}_j \cdot \boldsymbol{v}_k = 0, p \neq k, , p \neq j \qquad \boldsymbol{x} \in \partial x_j \quad \text{(A5f)}$$

where $\partial x_k$ is the boundary located at $x_k = 0$ and $x_k = 1/2$, $\partial x_j$ is the union of the boundaries located at $x_j = 0$ and $x_j = 1/2$ for $j \neq k$.

656

657 **7. References**
658


659 Aravena, J., M. Berli, S. Ruiz, F. Suarez, T. Ghezzehei, and S. Tyler (2014), Quantifying
660 coupled deformation and water flow in the rhizosphere using X-ray microtomography and
661 numerical simulations, *Plant and Soil*, *376*(1-2), 95-110.
662 Aravena, J. E., M. Berli, T. A. Ghezzehei, and S. W. Tyler (2011), Effects of Root-Induced
663 Compaction on Rhizosphere Hydraulic Properties - X-ray Microtomography Imaging and
664 Numerical Simulations, *Environmental Science & Technology*, *45*(2), 425-431.
665 Arbogast, T., and H. L. Lehr (2006), Homogenization of a Darcy–Stokes system modeling
666 vuggy porous media, *Computational Geosciences*, *10*(3), 291-302.
667 Blunt, M. J. (2001), Flow in porous media—pore-network models and multiphase flow,
668 *Current opinion in colloid & interface science*, *6*(3), 197-207.
669 Blunt, M. J., B. Bijeljic, H. Dong, O. Gharbi, S. Iglauer, P. Mostaghimi, A. Paluszny, and C.
670 Pentland (2013), Pore-scale imaging and modelling, *Advances in Water Resources*, *51*, 197-
671 216.
672 Bryant, S., and M. Blunt (1992), Prediction of relative permeability in simple porous media,
673 *Physical Review A*, *46*(4), 2004.
674 Bryant, S., D. Mellor, and C. Cade (1993a), Physically representative network models of
675 transport in porous media, *AIChE Journal*, *39*(3), 387-396.
676 Bryant, S., P. King, and D. Mellor (1993b), Network model evaluation of permeability and
677 spatial correlation in a real random sphere packing, *Transport in Porous Media*, *11*(1), 53-70.
678 Clausnitzer, V., and J. W. Hopmans (2000), Pore-scale measurements of solute breakthrough
679 using microfocus X-ray computed tomography, *Water Resources Research*, *36*(8), 2067-
680 2079.
681 Costanza-Robinson, M. S., K. H. Harrold, and R. M. Lieb-Lappen (2008), X-ray
682 microtomography determination of air− water interfacial area− water saturation relationships
683 in sandy porous media, *Environmental science & technology*, *42*(8), 2949-2956.
684 Crestana, S., S. Mascarenhas, and R. S. Pozzi-Mucelli (1985), Static and dynamic 3
685 dimensional studies of water in soil using computed tomographic scanning, *Soil Science*, *140*,
686 326-332.
687 Daly, K. R., and T. Roose (2014), Multiscale modelling of hydraulic conductivity in vuggy
688 porous media, *Proceedings of the Royal Society A: Mathematical, Physical and Engineering*
689 *Science*, *470*(2162).
690 Doube, M., M. M. Kłosowski, I. Arganda-Carreras, F. P. Cordelières, R. P. Dougherty, J. S.
691 Jackson, B. Schmid, J. R. Hutchinson, and S. J. Shefelbine (2010), BoneJ: Free and
692 extensible bone image analysis in ImageJ, *Bone*, *47*(6), 1076-1079.
693 Falconer, R. E., A. N. Houston, W. Otten, and P. C. Baveye (2012), Emergent Behavior of
694 Soil Fungal Dynamics: Influence of Soil Architecture and Water Distribution, *Soil Science*,
695 *177*(2), 111-119 110.1097/SS.1090b1013e318241133a.
696 Fatt, I. (1956), The network model of porous media.
697 Ferreira, T. A. W. R., and W. Rasband (2011), The ImageJ User Guide, Version 1.45.,
698 (http://rsbweb.nih.gov/ij/docs/user-guide.pdf).
699 Fowler, A. C. (1997), *Mathematical models in the applied sciences*, Cambridge University
700 Press, U.K.

Gao, W., T. Ren, A. G. Bengough, L. Auneau, C. W. Watts, and W. R. Whalley (2012), Predicting Penetrometer Resistance from the Compression Characteristic of Soil, *Soil Science Society of America Journal*, *76*(2), 361-369.
García-Marco, S., S. R. Ravella, D. Chadwick, A. Vallejo, A. S. Gregory, and L. M. Cárdenas (2014), Ranking factors affecting emissions of GHG from incubated agricultural soils, *European Journal of Soil Science*, *65*(4), 573-583.
Gardner, W. H. (1965), Water Content, in *Methods of Soil Analysis. Part 1. Physical and Mineralogical Properties, Including Statistics of Measurement and Sampling*, edited by C. A. Black, pp. 82-127, American Society of Agronomy, Soil Science Society of America.
Haugen, Å., N. Mani, S. Svenningsen, B. Brattekås, A. Graue, G. Ersland, and M. Fernø (2014), Miscible and Immiscible Foam Injection for Mobility Control and EOR in Fractured Oil-Wet Carbonate Rocks, *Transport in Porous Media*, *104*(1), 109-131.
Helliwell, J. R., A. J. Miller, W. R. Whalley, S. J. Mooney, and C. J. Sturrock (2014), Quantifying the impact of microbes on soil structural development and behaviour in wet soils, *Soil Biology and Biochemistry*, *74*(0), 138-147.
Hornung, U. (1997), *Homogenization and porous media*, Springer, Berlin, Germany.
Houston, A. N., W. Otten, P. C. Baveye, and S. Hapca (2013), Adaptive-window indicator kriging: A thresholding method for computed tomography images of porous media, *Computers & Geosciences*, *54*(0), 239-248.
Iassonov, P., T. Gebrenegus, and M. Tuller (2009), Segmentation of X-ray computed tomography images of porous materials: A crucial step for characterization and quantitative analysis of pore structures, *Water Resources Research*, *45*(9), W09415.
Keller, J. B. (1980), Darcy's law for flow in porous media and the two-space method, paper presented at Nonlinear partial differential equations in engineering and applied science (Proc. Conf., Univ. Rhode Island, Kingston, RI, 1979), Dekker New York.
Ketcham, R. A., and W. D. Carlson (2001), Acquisition, optimization and interpretation of X-ray computed tomographic imagery: applications to the geosciences, *Computers & Geosciences*, *27*(4), 381-400.
Keyes, S. D., K. R. Daly, N. J. Gostling, D. L. Jones, P. Talboys, B. R. Pinzer, R. Boardman, I. Sinclair, A. Marchant, and T. Roose (2013), High resolution synchrotron imaging of wheat root hairs growing in soil and image based modelling of phosphate uptake, *New Phytologist*, *198*(4), 1023-1029.
Mooney, S. J. (2002), Three-dimensional visualization and quantification of soil macroporosity and water flow patterns using computed tomography, *Soil Use and Management*, *18*(2), 142-151.
Mooney, S. J., and C. Morris (2008), A morphological approach to understanding preferential flow using image analysis with dye tracers and X-ray Computed Tomography, *CATENA*, *73*(2), 204-211.
Mooney, S. J., T. P. Pridmore, J. Helliwell, and M. J. Bennett (2012), Developing X-ray Computed Tomography to non-invasively image 3-D root systems architecture in soil, *Plant and Soil*, *352*(1-2), 1-22.
Panfilov, M. (2000), *Macroscale models of flow through highly heterogeneous porous media*, Springer.
Pavliotis, G., and A. Stuart (2008), *Multiscale Methods: Averaging and Homogenization*, Springer.
Ramstad, T., P. E. Oren, and S. Bakke (2010), Simulation of Two-Phase Flow in Reservoir Rocks Using a Lattice Boltzmann Method, *Spe Journal*, *15*(4), 923-933.
Reinhart, K. G. (1961), The Problem of Stones in Soil-Moisture Measurement1, *Soil Sci. Soc. Am. J.*, *25*(4), 268-270.

Rogasik, H., J. W. Crawford, O. Wendroth, I. M. Young, M. Joschko, and K. Ritz (1999), Discrimination of soil phases by dual energy x-ray tomography, *Soil Science Society of America Journal*, *63*(4), 741-751.
Rowell, D. L. (1994), *Soil science : methods and applications* Longman Scientific & Technical ; Prentice Hall.
Taylor, H. M., M. G. Huck, B. Klepper, and Z. F. Lund (1970), Measurement of Soil-grown Roots in a Rhizotron, *Agron. J.*, *62*(6), 807-809.
Tippkötter, R., T. Eickhorst, H. Taubner, B. Gredner, and G. Rademaker (2009), Detection of soil water in macropores of undisturbed soil using microfocus X-ray tube computerized tomography (μCT), *Soil and Tillage Research*, *105*(1), 12-20.
Tucker, C. (2014), Reduction of air- and liquid water-filled soil pore space with freezing explains high temperature sensitivity of soil respiration below 0 °C, *Soil Biology and Biochemistry*, *78*(0), 90-96.
van Genuchten, M. T. (1980), A Closed-form Equation for Predicting the Hydraulic Conductivity of Unsaturated Soils1, *Soil Sci. Soc. Am. J.*, *44*(5), 892-898.
Wildenschild, D., J. W. Hopmans, M. L. Rivers, and A. J. R. Kent (2005), Quantitative Analysis of Flow Processes in a Sand Using Synchrotron-Based X-ray Microtomography, *Vadose Zone J.*, *4*(1), 112-126.
Wildenschild, D., C. M. P. Vaz, M. L. Rivers, D. Rikard, and B. S. B. Christensen (2002), Using X-ray computed tomography in hydrology: systems, resolutions, and limitations, *Journal of Hydrology*, *267*(3–4), 285-297.
Zappala, S., J. R. Helliwell, S. R. Tracy, S. Mairhofer, C. J. Sturrock, T. Pridmore, M. Bennett, and S. J. Mooney (2013), Effects of X-Ray Dose On Rhizosphere Studies Using X-Ray Computed Tomography, *PLoS ONE*, *8*(6), e67250.

## 8. Figures

**Figure 1.** Outline of steps used in the subsampling, meshing and solution of cell problem. Figures (a) and (b) show the subsampling of a 1.2 mm side length cube of the segmented .stl file. Figure (c) shows the mesh generation. Figures (d) and (e) show the generation of a truly periodic geometry through translation (d) and reflection (e), the original volume mesh is shown in a lighter shade. Figure (f) shows the numerical solution for the local velocity magnitude in the subsampled soil.

**Figure 2.** Water release characteristic of the sand and clay sieved (a) and field structured (b) soils fitted to the van Genuchten (VG) curve. Error bars associated with histograms show one standard deviation. Note the different scaling on the y axis for figures (a) and (b).

**Figure 3.** Greyscale images showing examples of field structured (a) & (b) and sieved (c) & (d) clay (a) & (c) sand soil (b) & (d) at -75 kPa. Scale bar = 0.25 mm.

**Figure 4.** Hydraulic conductivity of field structured sand and clay soils averaged over all directions for decreasing j corresponding to increasing volume. The dots show the result from each of the cubic volumes, the lines show the average. The corresponding saturated hydraulic conductivity measured for the sand and clay soils are $1.3\times10^{-3}$ cm $s^{-1}$ and $0.4\times10^{-3}$ cm $s^{-1}$ respectively.

**Figure 5.** Hydraulic conductivity of field structured sand and clay soils as a function of matric potential.

**Figure 6.** 3D core section of a sand (a) and clay (b) soil sample at the specific matric potentials from saturation (left) to drier (right). Segmented phases are coloured brown (soil), blue (water filled pores) and black (air filled pores). Scale bar = 5 mm.

**Figure 7.** 3D pore thickness heat maps for a representative sand (a-c) and clay (e-f) sample at 0 (a, d), -20 (b, e) and -75 (c, f) kPa. (g) total air filled pore volume (bars) and average individual pore volumes (lines) for sand and clay soil. Error bars associated with histograms show one standard deviation.

**Figure 1.**

822

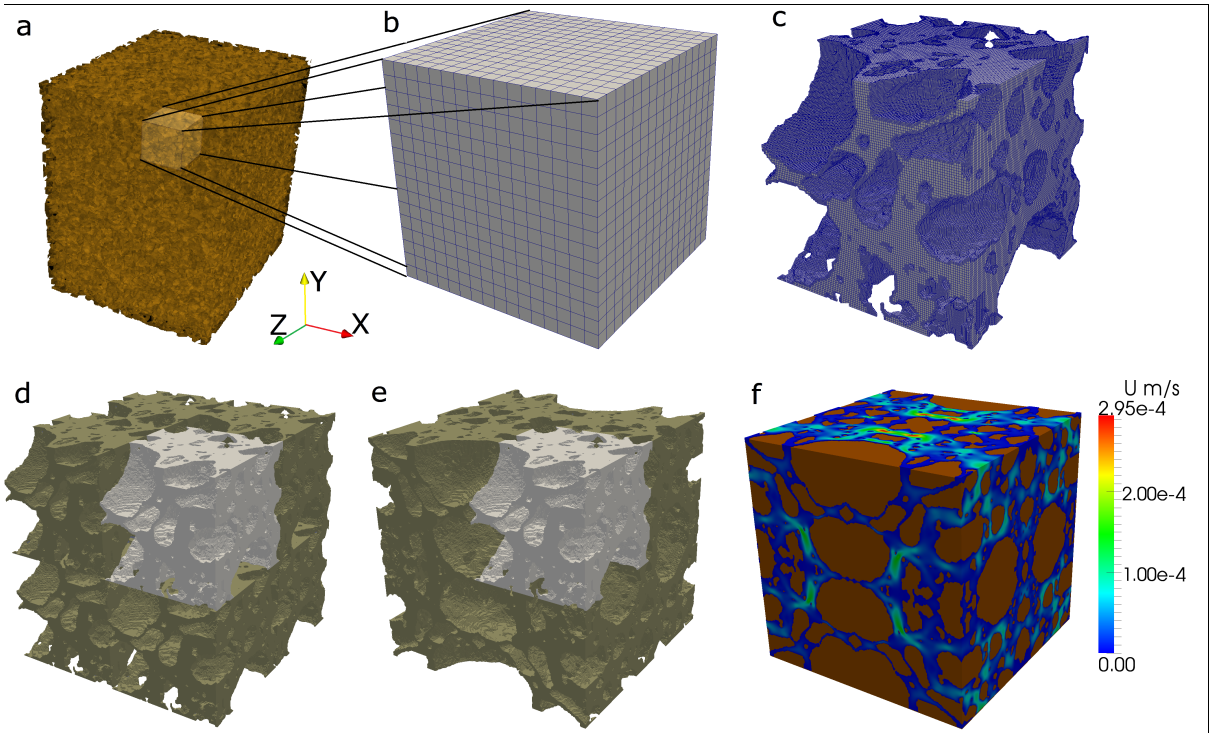


823